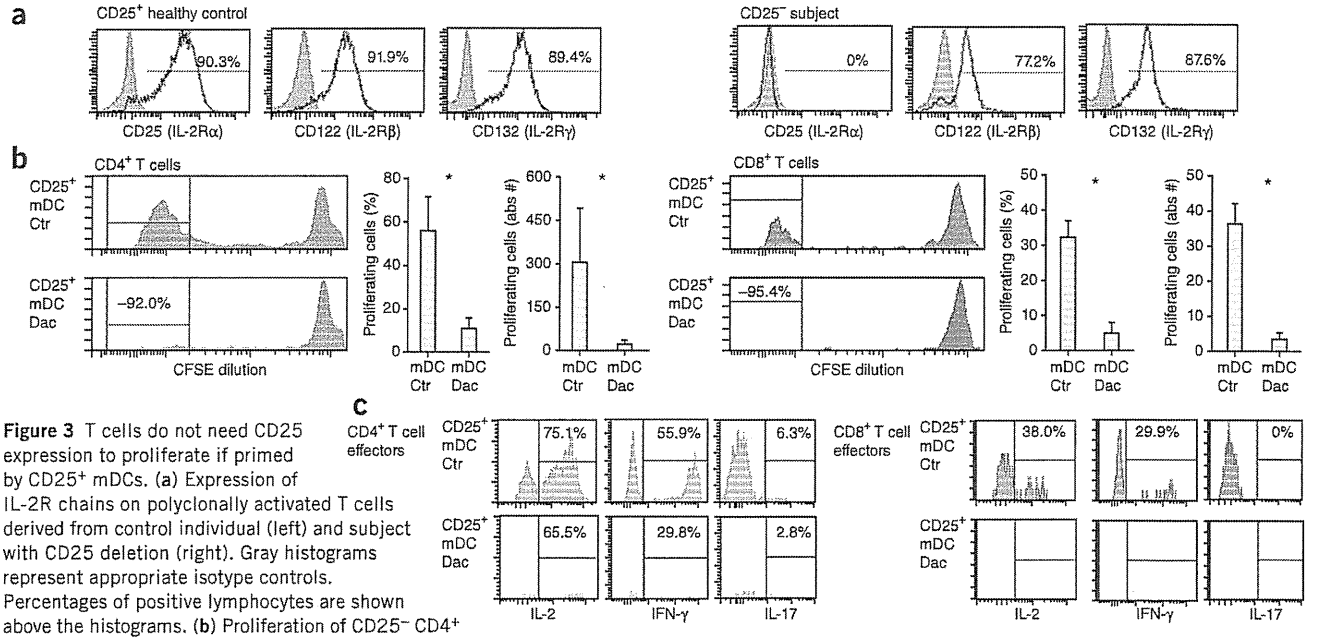

Figure 3 T cells do not need CD25 expression to proliferate if primed by CD25+ mDCs. (**a**) Expression of IL-2R chains on polyclonally activated T cells derived from control individual (left) and subject with CD25 deletion (right). Gray histograms represent appropriate isotype controls. Percentages of positive lymphocytes are shown above the histograms. (**b**) Proliferation of CD25− CD4+ (pink; left) and CD8+ (blue; right) T cells derived from an individual with a genetic deletion of CD25 after co-incubation with Flu-HA–loaded, human leukocyte antigen–matched CD25+ mDCs, as measured by CFSE dilution after 7 d. Separate graphs depict percentages and number of T cells normalized between conditions by fluorescent beads (abs #) of CD4+ and CD8+ T cells from four replicates; $*P < 0.05$. Mean values are shown ± s.d. (**c**) Cytokine production (IL-2, IFN-γ and IL-17) by proliferating CD25− CD4+ and CD8+ T cells after coculture with CD25+ mDCs (top) or mDCs pre-treated with daclizumab (bottom).

as mDCs expressed CD25. Pretreatment of mDCs with daclizumab before coculture with CD25− T cells caused more than 90% inhibition of T cell expansion, resulting in an almost complete lack of cytokine-producing effector cells (**Fig. 3b,c**).

Fab domain mediates inhibitory effect of daclizumab

To exclude the possibility that daclizumab binds mDCs via Fc receptors and then inhibits CD25 on primed T cells via the antigen-binding domain (Fab), we used a version of daclizumab that lacks the Fc fragment (Dac-Fab) and found that it has an equivalent inhibitory effect to whole daclizumab (**Supplementary Fig. 2**).

DCs lack IL-2Rβ and therefore do not signal to IL-2

As previous experiments showed that the inhibitory effect of daclizumab on T cell proliferation resided in its ability to block CD25 on mDCs, we investigated whether IL-2 binding to mDCs induces signaling. Another group has reported that human DCs may express high-affinity IL-2R and that daclizumab inhibits mDC function[22–24].

Thus, we investigated the expression of IL-2R chains in myeloid DCs. We analyzed blood dendritic cell antigen-1 (BDCA-1)+ DCs isolated from fresh human blood or apheresis samples (**Fig. 4a**) or monocyte-derived DCs (**Fig. 4b**) in their immature or mature stage and observed no expression of CD122 protein or mRNA (**Supplementary Fig. 3a**). Consequently, we observed no IL-2–induced Stat5 phosphorylation (**Fig. 4c**) in DCs from fresh human blood or *in vitro*–generated immature dendritic cells (iDCs) or mDCs. However, granulocyte-macrophage colony-stimulating factor (GM-CSF) induced Stat5 phosphorylation in all DC subsets (**Fig. 4d**; peak phopshorylated Stat5 (pStat5)+ DCs after 10–30 min of GM-CSF exposure: 86.9% in DCs present in fresh blood, 80.6% in iDCs and 51.2% in mDCs).

Even though we observed no Stat5 phosphorylation by DCs, we considered that IL-2 may provide a maturation signal to DCs through pathways other than Stat5 phosphorylation. However, we observed no effect on DC maturation of daclizumab, IL-2 or IL-2 in the presence of antibodies against the various chains of the IL-2R on DC maturation (**Supplementary Fig. 3b**). Finally, the previously reported effects on DC maturation of daclizumab on DCs[22–24] could be due to the formation of immune complexes between daclizumab and CD25 expressed on the surface of the few contaminating T cells in the DC preparation, as immune complexes can inhibit the stimulatory capacity of DCs[25]. We observed that, when added to the maturation stimulus, immune complexes significantly inhibited DC maturation and CD25 expression (**Supplementary Fig. 3b**).

mDCs use their CD25 to *trans*-present IL-2 to CD25− T cells

Because we observed no direct effect of IL-2 or daclizumab on DC maturation, we considered that, analogous to *trans*-presentation of IL-15 (ref. 26), mDCs might use their CD25 to complement the T cell expression of β and γ_c chains and facilitate assembly of the high-affinity IL-2R on T cells in *trans*.

To test this hypothesis, we first analyzed the time course of CD25 and IL-2 expression on polyclonally activated T cells. A small proportion of (memory) T cells produced IL-2 within the first hours after activation (**Supplementary Fig. 4**). However, these IL-2–producing T cells remained conspicuously CD25 negative for at least the first 10 h after activation. All T cells upregulated CD25 at later time points (≥24 h), but they also ceased to produce IL-2. This shutdown was IL-2 driven, as addition of IL-2–neutralizing antibody into T cell cultures restored IL-2 secretion (**Supplementary Fig. 4**). T cells activated in the presence of IL-2 resumed IL-2 production 48–72 h after stimulation, when they started to divide. The lack of CD25 expression on T cells within the first 10 h after activation supported our hypothesis that mDCs provide their CD25 to primed T cells for the formation of a high-affinity IL-2R. Thus, we tested the ability of mDCs to complement formation of high-affinity IL-2R on CD25− T cells.

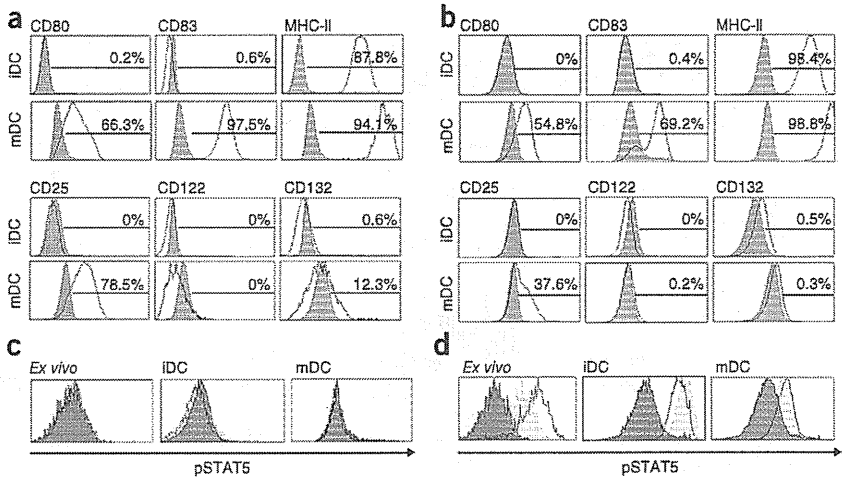

Figure 4 DCs do not express the β-chain of IL-2R and therefore do not signal in response to IL-2. (**a**) Flow cytometry analysis of freshly isolated BDCA-1$^+$ iDCs and mDCs (after 48 h of stimulation) stained for maturation markers CD80, CD83 and MHC-II (top, open histograms) and for IL-2R chains CD25, CD122 and CD132 (bottom, open histograms) or appropriate isotype controls (filled gray histograms). Percentages of surface marker expression are depicted above the histograms. (**b**) Flow cytometry analysis of *in vitro*–generated monocyte-derived iDCs and mDCs stained in an analogous manner to the cells in **a**. (**c**,**d**) STAT5 phosphorylation in response to 50 IU ml^{-1} of IL-2 (**c**) and 200 ng ml^{-1} of GM-CSF (**d**) of fresh uncoagulated whole blood (*ex vivo*, left), monocyte-derived iDCs (middle) and mDCs (right). Dark gray histograms represent appropriate isotype controls.

First we evaluated whether CD25$^+$ mDCs could restore Stat5 phosphorylation of daclizumab-pretreated T cells to exogenous IL-2 (**Supplementary Fig. 5**). In this system, we observed only very low (on average 9.86%; nonsignificant) restoration of IL-2 signaling. In contrast to IL-15Rα's high affinity for IL-2, CD25's low affinity for IL-2 precludes it from effectively capturing IL-2 in situations when IL-2 can freely diffuse to the surroundings. Thus, we hypothesized that mDCs release IL-2 into the immune synapse, facilitating effective capture of IL-2 by mDC-derived CD25 and its *trans*-presentation to a primed T cell. Because of the low precursor frequency of antigen-specific T cells in blood, we had to switch to antigen-experienced T cells. We selected a long-term CD4$^+$ T cell clone, P2-10 (ref. 27), specific for myelin basic protein ($MBP_{83–99}$) and several short-term (maximum 14 d from initial antigen-specific stimulation) CD4$^+$ T cell lines specific for Flu-$HA_{306–318}$, newly generated for each experiment. By including a short-term T cell line, we wanted to assure that no nonphysiological bias was introduced by long-term *in vitro* culture. We used these two antigen-specific systems interchangeably, loading syngeneic mDCs exogenously with cognate or noncognate peptide and confirmed our findings in both systems.

In the absence of exogenous IL-2, we observed strong Stat5 phosphorylation in T cells, which peaked 2 h after coculture with syngeneic mDCs loaded with cognate antigen (**Fig. 5** and **Supplementary Fig. 6a**). This Stat5 phosphorylation was significantly ($P < 0.05$) inhibited upon pretreatment of mDCs with daclizumab, whereas pretreatment of T cells with daclizumab had only a mild, nonsignificant inhibitory effect (**Fig. 5a** and **Supplementary Fig. 6a**). When we cocultured T cells with mDCs preloaded with noncognate antigen we observed no or little Stat5 phosphorylation, which was not amenable to inhibition by daclizumab. Notably, the level of mDC-induced Stat5 phosphorylation in T cells at this early stage of coculture correlated with the eventual expansion of antigen-specific effectors (**Fig. 5b** and **Supplementary Fig. 6b**). When we pooled data from multiple experiments, the Spearman's

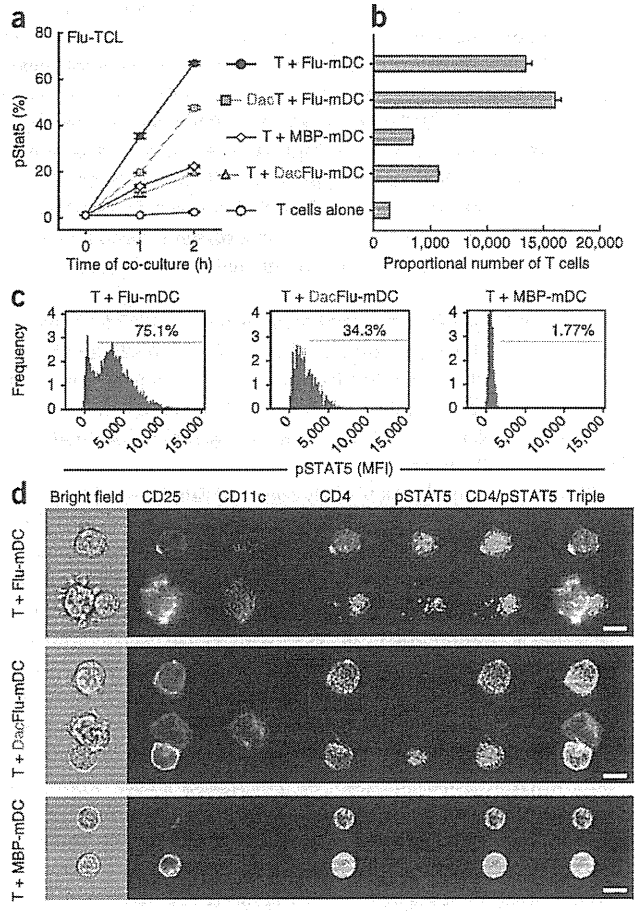

Figure 5 mDCs use their surface expression of CD25 to *trans*-present IL-2 to CD25$^-$ T cells (**a**) Phosphorylation of STAT5 in Flu-$HA_{306–318}$-specific T cells (TCL) selectively pretreated with daclizumab (DacT) or control Ab (T) and co-incubated with autologous, CD25-expressing mDCs pulsed with 1 μM cognate (Flu-mDC) or noncognate ($MBP_{83–99}$; MBP-mDC) peptide. At indicated conditions, Flu-mDCs were also pretreated with daclizumab (DacFlu-mDC). Results are depicted as percentages of pStat5-expressing CD4$^+$ T cells ± s.d. (**b**) The proportional number of expanded T cells after 5 d of coculture in the same cells and identical conditions as in **a**. Mean values are shown ± s.d. One representative experiment is depicted; all replicates are summarized in **Supplementary Figure 6**. (**c**) The frequency of pStat5$^+$ Flu-$HA_{306–318}$–specific T cells after 2 h culture with Flu-$HA_{306–318}$–loaded mDCs (left), daclizumab-pretreated, Flu-$HA_{306–318}$–loaded mDCs (middle) and $MBP_{83–99}$ peptide–loaded mDCs (right). MFI, mean fluorescence intensity. (**d**) pStat5 phosphorylation, as visualized by Amnis ImageStream in Flu-specific T cells cultured for 2 h with Flu-$HA_{306–318}$–loaded mDCs (top), daclizumab-pretreated Flu-$HA_{306–318}$-loaded mDCs (middle) or $MBP_{83–99}$-loaded mDCs (bottom) in the same cells as in **c**. Scale bars, 10 μm.

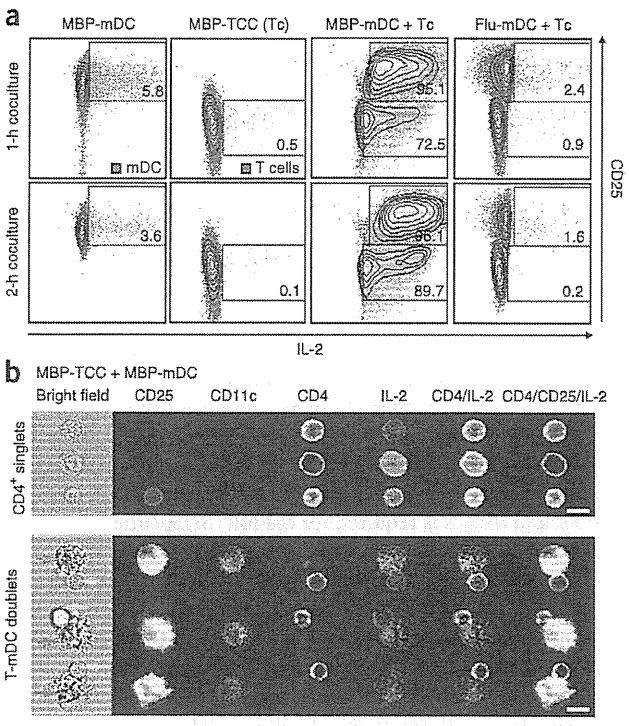

Figure 6 mDCs and T cells secrete IL-2 after antigen-specific interactions. (**a**) Flow cytometric analysis of IL-2 secretion of mDCs loaded with 1 μM $MBP_{83–99}$ peptide (MBP-mDC), MBP-specific T cell clones (MBP-TCC (Tc)), cocultures of MBP-mDCs with MBP-specific T cells (MBP-mDC + Tc) and cocultures of mDCs loaded with 1 μM Flu-$HA_{306–318}$ peptide with MBP-specific T cells (Flu-mDC + Tc). IL-2 was detected after 1 h (top) and 2 h (bottom) of coculture and is plotted against CD25 expression of mDCs and T cells. Percentages of IL-2 secretion by mDCs and T cells are shown in gates. For comparison, mDCs and T cells are presented in the same plot, but they were gated separately on CD11c and CD4 expression. (**b**) Independent experiment visualizing secreted IL-2 and surface expression of CD25, CD11c and CD4 by Amnis ImageStream after 2-h coculture of MBP-mDCs with MBP-specific T cells. Top, single MBP-specific $CD4^+$ T cells in the bright field of the microscope with simultaneous expression and/or secretion of fluorescently labeled CD25, CD4 and IL-2. Bottom, conjugates of MBP-loaded mDCs with MBP-specific T cells (mDCs highlighted by pink arrows, $CD4^+$ T cells by teal arrows). Scale bars, 10 μm.

correlation coefficient between Stat5 phosphorylation and subsequent T cell expansion was R = 0.875 with $P < 0.0001$.

To visualize formation of the immune synapse between T cells and mDCs, we used Amnis ImageStream technology, which allows visualization of mDC-T cell interactions with fluorescent microscopy and simultaneous quantification by flow cytometry (**Fig. 5c,d**). In this experiment, we observed minimal Stat5 phosphorylation of T cells cultured in the absence of mDCs (0.17%; data not shown) or cultured with syngeneic mDCs pulsed with noncognate antigen (1.77%; **Fig. 5c**). In contrast, coculture of T cells with cognate antigen–pulsed mDCs resulted in 75.1% $pStat5^+CD4^+$ T cells (**Fig. 5c**) and even greater T cell Stat5 phosphorylation (86.7%) when T cells were fixed in contact with mDCs. Virtually all mDCs in contact with T cells expressed CD25 (**Fig. 5d**). We also observed polarization of mDC-derived CD25 toward the immune synapse and the primed T cell. Pretreatment of mDCs with daclizumab resulted in decreased numbers of $pStat5^+$ T cells (34.3%; **Fig. 5c**), which was slightly higher than the proportion of T cells that expressed CD25 in this experiment (22.6–27.7%).

mDCs and T cells secrete IL-2 in an antigen-specific manner

As our previous experiment implied that the observed Stat5 phosphorylation was IL-2 driven, we wanted to visualize IL-2 secretion in mDC-T cell cocultures. Using an IL-2 secretion assay, in which the IL-2 secreted during cocultures is captured by an IL-2 catch reagent and later visualized on the surface of the cell that released it, we observed that very few mDCs and T cells secreted IL-2 when they were cultured alone (**Fig. 6a**). When the T cells were cultured in the presence of syngeneic mDCs loaded with cognate antigen, strong IL-2 secretion was induced both in mDCs and T cells (**Fig. 6a**) within the first 2 h of coculture. In contrast, coculture of T cells with mDCs loaded with noncognate antigen leads to a decrease in IL-2 secretion by mDCs even below baseline levels (**Fig. 6a**).

Visualization of IL-2 secretion by Amnis ImageStream (**Fig. 6b**) confirmed that either T cells or mDCs can be the source of secreted IL-2 in the antigen-specific system. Furthermore, IL-2 was secreted preferentially into the immune synapse, especially by mDCs, as visualized in enlarged images of the immune synapse (**Supplementary Fig. 7**).

DISCUSSION

Although DCs produce IL-2 after microbial stimulation[20,28], and the expression of CD25 is an activation marker on mDCs[21,22,29], the relevance of these observations for T cell activation has been unclear[30]. In agreement with mouse data[30,31], we observed that human myeloid DCs lack expression of IL-2R β chain (CD122), which is essential for IL-2 signaling[18]. Consequently, IL-2 failed to phosphorylate Stat5 in DCs and failed to affect the DC maturation phenotype. Therefore, we concluded that the CD25 on myeloid mDCs must have a different role than facilitating IL-2 signaling in DCs. We hypothesized that mDCs use their CD25 for targeted IL-2 delivery to primed T cells. This type of presentation in *trans* was already described for IL-15 (ref. 26), a cytokine closely related to IL-2, which uses identical intermediate affinity receptor chains. However, in contrast to the stable interaction of IL-15Rα with IL-15 (ref. 26), CD25 has low affinity for IL-2. Yet a biophysical model predicts that IL-2 binding of CD25 initiates the formation of a high-affinity IL-2R[16]. How can CD25 fulfill this key role under situations of low IL-2 concentration, such as at the initiation of the immune response, when pathogen-associated molecular pattern–activated mDCs may be the only source of IL-2? We hypothesized that directional secretion of IL-2 into the immune synapse would limit diffusion of IL-2 and facilitate its binding to CD25. Indeed, we observed strong Stat5 phosphorylation of T cells after coculture with syngeneic mDCs loaded with cognate antigen. Furthermore, the Stat5 phosphorylation in antigen-specific T cells was substantially inhibited by selective blockade of CD25 on the surface of mDCs. Stat5 phosphorylation was only slightly increased when T cells were cocultured with syngeneic $CD25^+$ mDCs loaded with noncognate antigen, probably owing to the fact that we observed no IL-2 secretion in such a setting. With antigen-experienced T cells, we observed that both mDCs and T cells secrete IL-2, although strictly in an antigen-specific manner. However, when we polyclonally activated resting T cells purified from human blood, we observed that only a small proportion of them were capable of secreting IL-2 within first 10 h after activation, and virtually none of those expressed CD25. We believe that this is more reminiscent of the priming of naive T cells; these T cells do not express CD25 and do not secrete IL-2 within the first few hours of antigen stimulation, making them entirely dependent on mDCs to facilitate their early IL-2 signaling. In contrast, memory/effector

T cells may contribute their own CD25, IL-2 or both when primed by mDCs, effectively lowering their stimulation requirements. Yet, the high-affinity IL-2 signal received during T cell priming seems to be a major determinant of subsequent T cell expansion, even for antigen-experienced T cells.

Our current model (**Supplementary Fig. 8**) predicts why immunodeficiency of adaptive T cell responses dominates the phenotype of humans with CD25 deficiency and coexists with paradoxical lymphoproliferation[7–9,32]. This model predicts that although CD25 deficiency would negatively affect development of antigen-specific effectors, it would not inhibit homeostatic T cell proliferation. Indeed, we observed that IL-7 can drive T cell proliferation in the presence of daclizumab, although it does not fully restore development of antigen-specific effectors (data not shown). Our model also explains the paradoxical observation that although complete (>99%) saturation of CD25 in blood lymphocytes is achieved with low doses of daclizumab (blood concentrations of 1 $\mu g\ ml^{-1}$), therapeutic efficacy increases with higher doses[4,33]. We predict that saturation of CD25 in lymph nodes and tissues is required for the full therapeutic effect of daclizumab in transplantation and autoimmunity.

In conclusion, our data have suggested a mechanism that highlights how the expression of cytokine signaling chains on various cells of the immune system can divergently regulate T cell functions through a single cytokine. This knowledge not only enhances understanding of the complexities of immunoregulation *in vivo* but also represents a basis for the development of more effective IL-2 and CD25-targeting therapies.

METHODS

Methods and any associated references are available in the online version of the paper at http://www.nature.com/naturemedicine/.

Note: Supplementary information is available on the Nature Medicine website.

ACKNOWLEDGMENTS

The study was supported by the intramural research program of the NINDS/NIH. We thank A. Kashani for expert technical assistance in processing apheresis samples and M. Lenardo, W. Leonard and H. McFarland for their critical review of the manuscript and helpful comments. Additionally, we are thankful to M. Lenardo and H. Su (NIH) for providing cryopreserved peripheral blood mononuclear cells (PBMCs) from the $CD25^-$ individual. Daclizumab F_{ab} was provided by Abbott Biotherapeutics, under Material Transfer Agreement.

AUTHOR CONTRIBUTIONS

B.B. developed the concept of the study and supervised the project. B.B. and T.A.W. designed the experiments. S.C.W., J.F.M., S.H., J.S.A.P., C.M.C., D.M., J.E., E.M. and B.B. performed the experiments and analyzed the data. B.B., S.C.W., J.F.M., S.H. and C.M.C. wrote the paper. All authors approved the final version of this paper.

COMPETING FINANCIAL INTERESTS

The authors declare competing financial interests: details accompany the full-text HTML version of the paper at http://www.nature.com/naturemedicine/.

Published online at http://www.nature.com/naturemedicine/.
Reprints and permissions information is available online at http://www.nature.com/reprints/index.html.

1. Waldmann, T.A. & O'Shea, J. The use of antibodies against the IL-2 receptor in transplantation. *Curr. Opin. Immunol.* **10**, 507–512 (1998).
2. Nussenblatt, R.B. *et al.* Treatment of noninfectious intermediate and posterior uveitis with the humanized anti-Tac mAb: a phase I/II clinical trial. *Proc. Natl. Acad. Sci. USA* **96**, 7462–7466 (1999).
3. Bielekova, B. *et al.* Humanized anti-CD25 (daclizumab) inhibits disease activity in multiple sclerosis patients failing to respond to interferon-β. *Proc. Natl. Acad. Sci. USA* **101**, 8705–8708 (2004).
4. Bielekova, B. *et al.* Effect of anti-CD25 antibody daclizumab in the inhibition of inflammation and stabilization of disease progression in multiple sclerosis. *Arch. Neurol.* **66**, 483–489 (2009).
5. Rose, J.W. *et al.* Daclizumab phase II trial in relapsing and remitting multiple sclerosis: MRI and clinical results. *Neurology* **69**, 785–789 (2007).
6. Willerford, D.M. *et al.* Interleukin-2 receptor α chain regulates the size and content of the peripheral lymphoid compartment. *Immunity* **3**, 521–530 (1995).
7. Sharfe, N., Dadi, H.K., Shahar, M. & Roifman, C.M. Human immune disorder arising from mutation of the α chain of the interleukin-2 receptor. *Proc. Natl. Acad. Sci. USA* **94**, 3168–3171 (1997).
8. Aoki, C.A. *et al.* IL-2 receptor α deficiency and features of primary biliary cirrhosis. *J. Autoimmun.* **27**, 50–53 (2006).
9. Roifman, C.M. Human IL-2 receptor α chain deficiency. *Pediatr. Res.* **48**, 6–11 (2000).
10. Morgan, D.A., Ruscetti, F.W. & Gallo, R. Selective in vitro growth of T lymphocytes from normal human bone marrows. *Science* **193**, 1007–1008 (1976).
11. Setoguchi, R., Hori, S., Takahashi, T. & Sakaguchi, S. Homeostatic maintenance of natural Foxp3+ CD25+ CD4+ regulatory T cells by interleukin (IL)-2 and induction of autoimmune disease by IL-2 neutralization. *J. Exp. Med.* **201**, 723–735 (2005).
12. Lenardo, M.J. Interleukin-2 programs mouse T lymphocytes for apoptosis. *Nature* **353**, 858–861 (1991).
13. Martin, J.F., Perry, J.S., Jakhete, N.R., Wang, X. & Bielekova, B. An IL-2 paradox: blocking CD25 on T cells induces IL-2–driven activation of CD56(bright) NK cells. *J. Immunol.* **185**, 1311–1320 (2010).
14. Oh, U. *et al.* Regulatory T cells are reduced during anti-CD25 antibody treatment of multiple sclerosis. *Arch. Neurol.* **66**, 471–479 (2009).
15. Bielekova, B. *et al.* Regulatory CD56(bright) natural killer cells mediate immunomodulatory effects of IL-2R-α–targeted therapy (daclizumab) in multiple sclerosis. *Proc. Natl. Acad. Sci. USA* **103**, 5941–5946 (2006).
16. Wang, X., Rickert, M. & Garcia, K.C. Structure of the quaternary complex of interleukin-2 with its α, β and γc receptors. *Science* **310**, 1159–1163 (2005).
17. Leonard, W.J. *et al.* Signaling via the IL-2 and IL-7 receptors from the membrane to the nucleus. *Cold Spring Harb. Symp. Quant. Biol.* **64**, 417–424 (1999).
18. Malek, T.R. The biology of interleukin-2. *Annu. Rev. Immunol.* **26**, 453–479 (2008).
19. Granucci, F., Zanoni, I., Feau, S. & Ricciardi-Castagnoli, P. Dendritic cell regulation of immune responses: a new role for interleukin 2 at the intersection of innate and adaptive immunity. *EMBO J.* **22**, 2546–2551 (2003).
20. Granucci, F. *et al.* Inducible IL-2 production by dendritic cells revealed by global gene expression analysis. *Nat. Immunol.* **2**, 882–888 (2001).
21. Velten, F.W., Rambow, F., Metharom, P. & Goerdt, S. Enhanced T-cell activation and T-cell–dependent IL-2 production by CD83+, CD25high, CD43high human monocyte-derived dendritic cells. *Mol. Immunol.* **44**, 1544–1550 (2007).
22. Mnasria, K., Lagaraine, C., Manaa, J., Lebranchu, Y. & Oueslati, R. Anti CD25 treatment of human dendritic cells modulates both their cytokine synthesis profiles and their capacity to activate allogeneic CD4 T cells: a potential tolerogenic effect. *Int. Immunopharmacol.* **8**, 414–422 (2008).
23. Mnasria, K., Lagaraine, C., Velge-Roussel, F., Lebranchu, Y. & Baron, C. Anti-CD25 antibodies decrease the ability of human dendritic cells to prime allogeneic CD4 T cells. *Transplant. Proc.* **41**, 695–697 (2009).
24. Mnasria, K. *et al.* Anti-CD25 antibodies affect cytokine synthesis pattern of human dendritic cells and decrease their ability to prime allogeneic CD4+ T cells. *J. Leukoc. Biol.* **84**, 460–467 (2008).
25. Siragam, V. *et al.* Intravenous immunoglobulin ameliorates ITP via activating Fcγ receptors on dendritic cells. *Nat. Med.* **12**, 688–692 (2006).
26. Dubois, S., Mariner, J., Waldmann, T.A. & Tagaya, Y. IL-15Rα recycles and presents IL-15 in *trans* to neighboring cells. *Immunity* **17**, 537–547 (2002).
27. Bielekova, B. *et al.* Encephalitogenic potential of the myelin basic protein peptide (amino acids 83–99) in multiple sclerosis: results of a phase II clinical trial with an altered peptide ligand. *Nat. Med.* **6**, 1167–1175 (2000).
28. Slack, E.C. *et al.* Syk-dependent ERK activation regulates IL-2 and IL-10 production by DC stimulated with zymosan. *Eur. J. Immunol.* **37**, 1600–1612 (2007).
29. Strowig, T. *et al.* Tonsilar NK cells restrict B cell transformation by the Epstein-Barr virus via IFN-γ. *PLoS Pathog.* **4**, e27 (2008).
30. Kronin, V., Vremec, D. & Shortman, K. Does the IL-2 receptor α chain induced on dendritic cells have a biological function? *Int. Immunol.* **10**, 237–240 (1998).
31. Létourneau, S., Krieg, C., Pantaleo, G. & Boyman, O. IL-2- and CD25-dependent immunoregulatory mechanisms in the homeostasis of T-cell subsets. *J. Allergy Clin. Immunol.* **123**, 758–762 (2009).
32. Caudy, A.A., Reddy, S.T., Chatila, T., Atkinson, J.P. & Verbsky, J.W. CD25 deficiency causes an immune dysregulation, polyendocrinopathy, enteropathy, X-linked–like syndrome and defective IL-10 expression from CD4 lymphocytes. *J. Allergy Clin. Immunol.* **119**, 482–487 (2007).
33. Wynn, D. *et al.* Daclizumab in active relapsing multiple sclerosis (CHOICE study): a phase 2, randomised, double-blind, placebo-controlled, add-on trial with interferon β. *Lancet Neurol.* **9**, 381–390 (2010).
34. Cartagena, C.M., Burns, M.P. & Rebeck, G.W. 24S-hydroxycholesterol effects on lipid metabolism genes are modeled in traumatic brain injury. *Brain Res.* **1319**, 1–12 (2010).

Chronic Multiple Sclerosis Lesions: Characterization with High-Field-Strength MR Imaging[1]

Bing Yao, PhD
Francesca Bagnato, MD, PhD
Eiji Matsuura, MD, PhD
Hellmut Merkle, PhD
Peter van Gelderen, PhD
Fredric K. Cantor, MD
Jeff H. Duyn, PhD

Purpose: To elucidate the mechanism of magnetic resonance (MR) imaging contrast in multiple sclerosis (MS) lesion appearance by using susceptibility-weighted imaging and to assess with histologic correlation the role of iron and myelin in generating this MR imaging contrast.

Materials and Methods: Each patient provided written consent to a human subject protocol approved by an institutional review board. High-spatial-resolution susceptibility-weighted 7.0-T MR images were obtained in 21 patients with MS. Contrast patterns in quantitative phase and R2* images, derived from 7.0-T data, were investigated in 220 areas defined as chronic MS lesions on conventional T2-weighted fluid-attenuated inversion recovery, T2-weighted, and T1-weighted spin-echo images. The presence of positive or negative phase shifts (ie, decreased or increased MR frequency, respectively) was assessed in each lesion. In addition, postmortem MR imaging was performed at 7.0 T and 11.7 T, and its results were correlated with those of immunohistochemical staining specific for myelin, iron, and ferritin.

Results: The majority (133 [60.5%] of 220) of the identified lesions had a normal phase and reduced R2*. A substantial fraction of the lesions (84 [38.2%] of 220) had negative phase shift, either uniformly or at their rim, and a variety of appearances on R2* maps. These two lesion contrast patterns were reproduced in the postmortem MR imaging study. Comparison with histologic findings showed that, while R2* reduction corresponded to severe loss of both iron and myelin, negative phase shift corresponded to focal iron deposits with myelin loss.

Conclusion: Combined analysis of 7.0-T R2* and phase data may help in characterizing the pathologic features of MS lesions. The observed R2* decreases suggest profound myelin loss, whereas negative phase shifts suggest a focal iron accumulation.

Supplemental material: *http://radiology.rsna.org/lookup/suppl/doi:10.1148/radiol.11110601/-/DC1*

[1] From the Advanced MRI Section (B.Y., H.M., P.v.G., J.H.D.), Laboratory of Functional Molecular Imaging, and Neuroimmunology Branch (E.M., F.K.C.), Neurologic Disorders and Stroke, National Institutes of Health, 10 Center Dr, Bldg 10, Room B1D728, MSC 1065, Bethesda, MD 20892-1065; and Department of Radiology, Institute of Imaging Science, Vanderbilt University, Nashville, Tenn (F.B.). Received March 22, 2011; revision requested June 1; revision received July 27; accepted August 3; final version accepted August 15. **Address correspondence to** B.Y. (e-mail: *yaob@mail.nih.gov*).

Magnetic resonance (MR) imaging is the most powerful preclinical tool for diagnosing and monitoring over time patients with multiple sclerosis (MS). MR imaging is particularly sensitive to the white matter (WM) disease associated with MS because WM changes affect many measurable MR imaging parameters, including proton density (1,2), water diffusion (3), T1 and T2 relaxation times (4–6), and cross relaxation (7,8). Changes in these parameters are interpreted as indicators of myelin and axon loss, which may follow the initial inflammatory process in MS-induced WM lesions.

Over the past few years, ultra-high-field-strength MR imaging systems have become available for clinical research. Owing to combined gains in image contrast and spatial resolution as compared with lower field strength systems, imaging at ultra high fields, including 7.0 T, has the potential to improve the understanding of diseases such as MS. Recent work (9,10) has shown that high-field-strength MR imaging based on magnetic susceptibility contrast may be exquisitely sensitive to MS pathologic features, offering the possibility of improved detection and characterization of the disease. Specifically, strong contrast has been observed in magnitude and phase images of susceptibility-weighted (so-called T2*-weighted) MR imaging examinations. Contrast in susceptibility-weighted images is sensitive to the apparent transverse relaxation time constant (ie, T2*) and resonance frequency shifts of the MR imaging signal induced by local variations in parenchymal magnetic susceptibility. Such susceptibility-weighted contrast has been shown to be highly variable, both within lesions and among different MS lesions in the same patient. This variability may reflect distinct pathologic processes.

Recent studies (11–20) of healthy brains both in vivo and postmortem suggest that magnetic susceptibility contrast may have a number of contributors, including myelin and both heme iron (deoxyhemoglobin) and nonheme iron. The tissue concentration of nonheme iron and myelin are particularly relevant to MS as they may be reflective of the underlying disease process (21). However, it is not clear to what extent iron and myelin contribute to the variable contrast seen in susceptibility-weighted MR imaging. To investigate this, we studied the in vivo and postmortem appearance of MS lesions in susceptibility-weighted high-field-strength MR imaging and compared the findings with those of histochemical staining for iron and myelin.

The purpose of the present study was to elucidate the mechanism of contrast underlying MS lesion appearance at susceptibility-weighted MR imaging and to assess, with histologic demonstration, the role of iron and myelin in generating this MR imaging contrast.

Advances in Knowledge

- The majority (133 [60.5%] of 220) of identified white matter lesions in patients with multiple sclerosis (MS) at 7.0-T MR imaging have a normal resonance frequency and a reduced R2* value.
- A substantial fraction of MS lesions (84 [38.2%] 220) show increased MR imaging resonance frequency either uniformly or at their periphery, as well as variable R2* values.
- Comparison with histologic findings showed that R2* reduction corresponded to severe loss of both iron and myelin, while resonance frequency increases corresponded to focal iron deposits with myelin loss.

Materials and Methods

In Vivo Study

Study design and patients.—Twenty-four patients (12 men and 12 women; mean age, 46.2 years; range, 28–60 years) with clinically definite MS in accordance with the revised McDonald criteria (22) were included in the study. Each patient provided written consent to a human subject protocol approved by the National Institute of Neurological Disorders and Stroke review board. Detailed patient demographic information is provided in Table 1 (note that three patients were excluded from the patient statistics owing to poor data quality). This retrospective study was performed between January 2009 and December 2010. Within 3 weeks (range, 1–3 weeks), each patient underwent 7.0-T MR imaging and a physical examination to rate disability by using the EDSS (23). Together with the 7.0-T examination, 3.0-T MR imaging was also performed to provide an independent standard for definition of lesions. Patient inclusion and exclusion criteria are as follows: Patients had to be 18–65 years old (inclusive) and free of clinical relapse for at least 3 months at the time of the study. Patients with an EDSS score greater than 6.5 were not included owing to

Implication for Patient Care

- Combined analysis of R2* and phase data at 7.0 T may help in characterizing the pathologic features of MS lesions.

Published online before print
10.1148/radiol.11110601 **Content code:** NR

Radiology 2012; 262:206–215

Abbreviations:
EDSS = Expanded Disability Status Scale
FLAIR = fluid-attenuated inversion recovery
MS = multiple sclerosis
RR = relapsing-remitting
WM = white matter

Author contributions:
Guarantors of integrity of entire study, B.Y., H.M., J.H.D.; study concepts/study design or data acquisition or data analysis/interpretation, all authors; manuscript drafting or manuscript revision for important intellectual content, all authors; manuscript final version approval, all authors; literature research, B.Y., F.B., H.M., J.H.D.; clinical studies, B.Y., F.B.; experimental studies, B.Y., F.B., E.M., H.M., P.v.G., J.H.D.; statistical analysis, B.Y., F.B.; and manuscript editing, all authors

Funding:
This research was supported by the intramural program of the National Institute of Neurological Disorders and Stroke at the National Institutes of Health.

Potential conflicts of interest are listed at the end of this article.

limitations of access to the MR imaging table. Further details of the exclusion criteria are provided in Appendix E1 (online).

MR imaging.—MR imaging acquisition was performed by two authors (B.Y., with 8 years of experience in MR imaging, and F.B., with 15 years of experience in MR imaging and MS). The 7.0-T examination was performed with an MR imaging unit (GE Medical Systems, Milwaukee, Wis) equipped with a 32-channel detector array (Nova Medical, Wilmington, Mass). To improve temporal signal stability, a real-time modulation of magnetic field shims (up to second order) was performed to compensate for respiration-induced magnetic field changes in the brain (24).

MR imaging with magnetic susceptibility contrast was performed by using a high-spatial-resolution two-dimensional multiecho gradient-echo sequence with the parameters in Table 2. A sensitivity encoding acceleration rate of two was used to minimize the imaging time.

The 3.0-T examination was performed with an MR imaging unit (GE Medical Systems) equipped with an eight-channel head coil. The acquisitions included the following two-dimensional sequences: T2-weighted FLAIR, T2-weighted spin echo, and T1-weighted spin echo, performed before and 10 minutes after the intravenous injection of 0.1 mmol of gadopentetate dimeglumine (Magnevist; Schering, Berlin, Germany) per kilogram of body weight. The imaging parameters are listed in Table 2.

Image analysis.—Image analysis was performed by one author (B.Y.). The 7.0-T images for each echo time were reconstructed by using a phase-sensitive noise-weighted channel combination (25). Quantitative R2* maps were obtained by using exponential fitting to the images acquired at a range of echo times. To remove phase wraps, the complex data were first smoothed by a Gaussian filter (full width at half maximum, 30 voxels) to determine the macroscopic background phase. Continuous phase maps were then generated after subtraction of the phase background from the original data. Negative phase shifts (darkening in the maps) corresponded to increased MR imaging resonance frequency, generally indicating paramagnetic susceptibility shifts. Data processing was performed with software code created in house by using Interactive Data Language, version 7.0 (ITT Visual Information Solutions, White Plains, NY).

In each patient, 3.0-T images (T1-weighted spin echo, T2-weighted spin echo, and FLAIR) were registered to the 7.0-T gradient-echo image by using the coregistration algorithm implemented in SPM8 (Wellcome Trust Centre for Neuroimaging, London, England). Detailed procedures are discussed in Appendix E1 (online).

Lesion identification and classification.—The lesions were identified on 7.0-T R2* and phase maps. To ensure that only lesions defined at conventional 3.0-T MR imaging were included in the study, all the lesions identified at 7.0 T were counted as lesions if they were confirmed as hyperintense WM lesions on T2-weighted spin-echo and T2-weighted FLAIR images at 3.0 T (26). Lesion identification at 7.0 T was performed by two authors (B.Y. and F.B.). In case of disagreement, the opinion of an expert senior investigator (J.H.D., with 29 years of experience in MR imaging) was sought and followed. On the basis of their appearance in the 7.0-T phase and R2* images, and as in previous work (9), a distinction was made between lesions that had uniform intensity and lesions that had pronounced rim contrast. For both R2* and phase maps, the lesions were classified into the following five categories: *(a)* Hypointense lesions, which showed hypointense signal throughout the lesion compared with the surrounding normal-appearing WM (NAWM); *(b)* hyperintense lesions, which showed hyperintense signal throughout the lesion compared with the surrounding NAWM; *(c)* hypointense-rim lesions, which showed a hypointense rim signal while being either hyper- or isointense in their inner portion; *(d)* hyperintense-rim lesions, which showed hyperintense rim signal while being either hypo- or isointense in their inner portion; and *(e)* isointense lesions, which showed normal contrast compared with the surrounding tissue.

Table 1

Demographic, Clinical, and MR Imaging Characteristics in 21 Patients

Parameter	Male Patients (n = 11)	Female Patients (n = 10)
Age (y)	47.0 ± 8.3 (36–60)	43.2 ± 11.0 (28–57)
EDSS score*	2.2 (1–6)	1.9 (0–6)
MS type		
RR	10	9
SP	1	1
Disease duration (y)	11.3 ± 9.0 (0.3–25)	12.2 ± 10.5 (0.1–33)
No. of contrast-enhancing lesions	1 In 1 patient	1 In 1 patient

Note.—Unless otherwise specified, data are means ± standard deviations, with ranges in parentheses. EDSS = Expanded Disability Status Scale, RR = relapsing-remitting, SP = secondary progressive.

* Data are medians, with ranges in parentheses.

Postmortem Study

The postmortem MS specimen used in this study was obtained from a 70-year-old man, who died of pneumonia linked to secondary progressive MS. Details of his clinical history have been described previously (2). Briefly, at the time of his death, the patient was bedridden (EDSS score, 8.5) and had had MS for more than 30 years.

Within a few hours after death, the cadaver was brought for autopsy. The brain was removed and immediately fixed in 4% formalin for 2 weeks; it was then cut into 10-mm-thick coronal slices. Each slice was fixed in 4% formalin until imaging. MR images were obtained 36 months after death.

Table 2

MR Imaging Parameters

Parameter	In Vivo 3.0-T Imaging			In Vivo Multiecho Gradient-Echo 7.0-T Imaging	Postmortem 3D Multiecho Gradient-Echo 11.7-T Imaging
	T2-weighted FLAIR Sequence	T2-weighted Spin-Echo Sequence	T1-weighted Spin-Echo Sequence		
Spatial resolution (mm)	0.43 × 0.43	0.43 × 0.43	0.86 × 0.86	0.31 × 0.31	0.1 × 0.1
Echo time(s) (msec)	140	120	11	15.5, 30.0, 44.5	3.9, 10.4, 16.9, 23.4
Repetition time (msec)	8800	5300	700	2000	40
Inversion time (msec)	2200	NA	NA	NA	NA
Section thickness/spacing (mm)	3/0	3/0	3/0	0.8/0.2	0.1/0
Bandwidth (kHz)	62.5	125	50	62.5	75
Imaging time	5 Min	2 Min	5 Min	9.5 Min per slab for 3 slabs	12 H 17 mins for average of 12 acquisitions

Note.—FLAIR = fluid-attenuated inversion recovery, NA = not applicable, 3D = three-dimensional.

Table 3

Lesion Appearance at 7.0 T

Appearance on Phase Images	Appearance on R2* Images					
	Hypointense	Hyperintense	Hyperintense Rim	Hypointense Rim	Isointense	Total
Hypointense	30 (13.6)	8 (3.6)	5 (2.3)	0	25 (11.4)	68 (30.1)
Hypointense rim	7 (3.2)	0	8 (3.6)	0	1 (0.5)	16 (7.3)
Hyperintense rim	1 (0.5)	0	0	1 (0.5)	1 (0.5)	3 (1.4)
Isointense	133 (60.5)	0	0	0	0	133 (60.5)
Total	171 (77.7)	8 (3.6)	13 (5.9)	1 (0.5)	27 (12.3)	220 (100)

Note.—Data are numbers of lesions, with percentages in parentheses.

Postmortem MR imaging.—Each brain slice was placed into flat, cylindric, custom-fabricated tissue containers (2) and was imaged in 4% formalin solution. The MR imaging examination was performed with the human 7.0-T imaging unit, which was equipped with a 24-channel receive-only detector array specifically designed for imaging these tissue slabs. A three-dimensional multiecho gradient-echo sequence was performed with the following parameters: echo times, 8.7, 25.2, 41.7, and 58.2 msec; repetition time, 200 msec; spatial resolution, 0.2-mm isotropic; and flip angle = 20°. After inspection of the reconstructed images, a few characteristic lesion areas were cut into 2 × 2 × 1-cm^3 pieces and imaged with the 11.7-T MR imaging unit (Bruker BioSpin, Ettlingen, Germany) with 0.1 mm isotropic resolution and echo times of 3.9, 10.4, 16.9, and 23.4 msec (see Table 2 for detailed imaging parameters). The R2* and phase maps were calculated by using the same methods used in the in vivo experiments.

Immunohistochemistry.—After MR imaging, the brain was embedded in paraffin. Small segments (2 × 4 × 3 mm^3 each) were cut in 10-μm-thick serial slices with a microtome (Carl Zeiss MicroImaging, Thornwood, NY) and mounted onto Superfrost glass slides (Thermo Fisher Scientific, Waltham, Mass). Sections were deparaffinized prior to histologic staining. Perls staining for iron and standard Luxol fast blue staining for myelin, as well as immunochemical antibody staining for ferritin, were performed on consecutive slices, and the results were compared with MR images. Control stains were also performed with each type of stain. Details of the staining procedures used in this study are discussed in Appendix E1 (online).

Results

In Vivo Results

Data in three patients had to be excluded from the analysis because of severe image artifacts related to head movements during the acquisition. Good-quality susceptibility-weighted MR imaging data were obtained in the remaining 21 patients with MS. The majority of the patients had RR MS in a stable phase (ie, no active lesions). A total of two contrast-enhancing lesions were seen in two patients after gadopentetate dimeglumine injection, suggesting acute lesions. These two lesions were excluded from our analysis, which focused only on chronic lesions.

Both magnitude and phase images showed a varied appearance of MS lesions within and across patients. This variation was also observed in the R2* data and, to a lesser extent, in the conventional T1- and T2-weighted data obtained at 3.0 T (Figs 1–3). Table 3 reports the details of the chronic lesion classification, including the distinction between lesions with and lesions without rim contrast on the 7.0-T images. A total of 220 sharp and demarcated focal lesions were counted on the 7.0-T R2* and phase images in all the patients. All of these lesions were hyperintense on

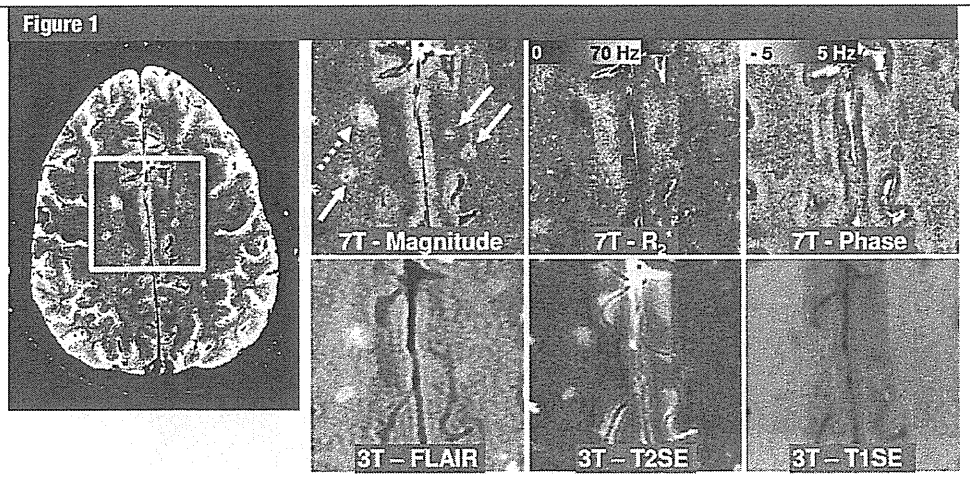

Figure 1: Transverse MR images in 50-year-old woman with RR MS, an EDSS score of 1.0, and 22 years of disease show nodular lesions with uniform interior. Lesion contrast varies across various image types, including susceptibility-weighted magnitude, phase, and R2* images obtained at 7.0 T and FLAIR, T2-weighted spin-echo *(T2SE)*, and T1-weighted spin-echo *(T1SE)* images obtained at 3.0 T. Intensity scaling of each image was adjusted to accentuate the lesions. Three lesions (solid arrows) appear in all image types; a fourth one (dotted arrow) appears in all images except the phase image.

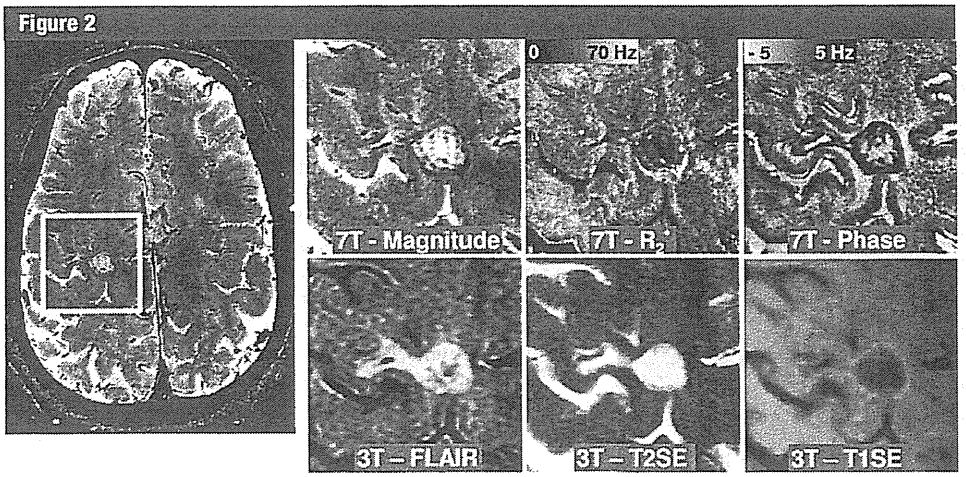

Figure 2: Transverse MR images in 40-year-old man with RR MS, an EDSS score of 2.5, and 7.5 years of disease show lesion with inhomogeneous intensity and contrast at its rim. Lesion contrast varies across various image types, including susceptibility-weighted magnitude, phase, and R2* images obtained at 7.0 T and FLAIR, T2-weighted spin-echo *(T2SE)*, and T1-weighted spin-echo *(T1SE)* images obtained at 3.0 T. Intensity scaling of each image was adjusted to accentuate the lesions.

the T2-weighted spin-echo and FLAIR images.

Most lesions had a reduced R2* and normal phase (133 [60.5%] of 220) or a reduced R2* and negative phase shift (30 [13.6%] of 220 [Table 3]). Of the 171 lesions with reduced R2*, 130 (76.0%) appeared as hypointense lesions on 3.0-T T1-weighted images; these are also known as "T1 black hole" lesions (27). A substantial fraction of the lesions (total, 84 [38.2%] of 220) had negative phase shift, either uniformly (68 [30.1%] of 220) or at their rim (16 [7.3%] of 220), and a variety of appearances on R2* maps. Twenty-five (11.4%) of the 220 lesions had a normal R2* and negative phase shift. Sixteen (7.3%) of the 220 lesions showed negative phase shift at their periphery (ring-type lesions). This lesion type occurred in 10 of the 21 patients. The negative phase shift coincided with either a normal or an increased R2* at the rim. Of the 16 lesions with rim contrast, 15 (93.8%) had reduced intensity (ie, were T1 black holes) on T1-weighted spin-echo images. No positive phase shift lesions were found among the 220 total lesions; therefore, there is no "hyperintense" row in Table 3.

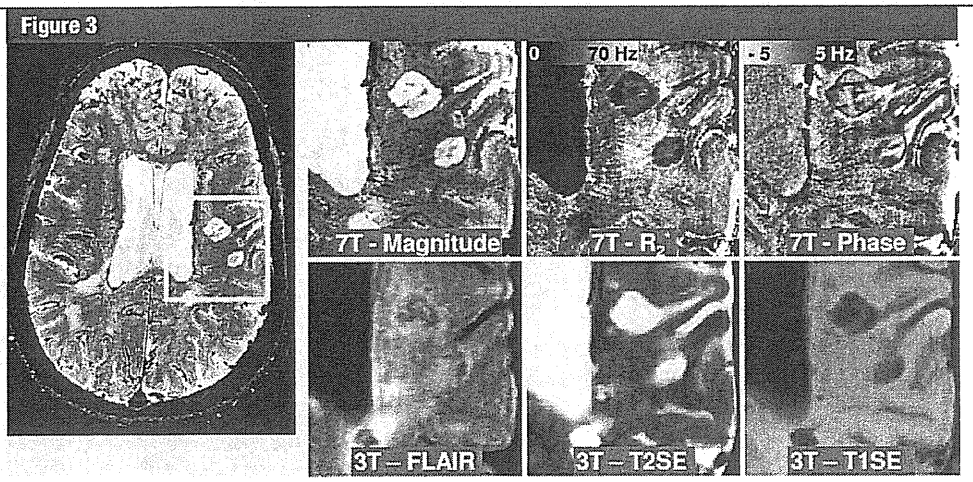

Figure 3: Transverse MR images in 49-year-old woman with RR MS, an EDSS score of 4, and 20.2 years of disease show ring-type lesions. Lesion contrast varies across various image types, including susceptibility-weighted magnitude, phase, and R2* images obtained at 7.0 T and FLAIR, T2-weighted spin-echo *(T2SE)*, and T1-weighted spin-echo *(T1SE)* images obtained at 3.0 T. Intensity scaling of each image was adjusted to accentuate the lesions.

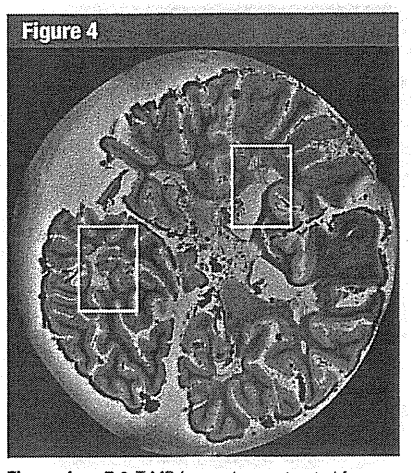

Figure 4: 7.0-T MR image (reconstructed from a three-dimensional gradient-echo image with 0.2-mm isotropic resolution, an echo time of 25.2 msec, and a repetition time of 200 msec) of postmortem tissue sample used for histologic comparison. Rectangles = areas selected for further analysis, results of which are shown in Figures 5 and 6.

Examples of these most prevalent lesion types are shown in Figures 1–3. Figure 1 shows examples of four typical lesions with R2* decrease, three of which also had negative phase shift. The lesions are visible on the 3.0-T FLAIR and T2-weighted spin-echo images as well and are faintly visible on the T1-weighted spin-echo image. Figure 2 shows an example of lesion whose signal is relatively uniform on the T2-weighted spin-echo image but has a decreased R2* in the inner portion and a negative phase shift at its rim. A hyperintense rim is also visible on the T1-weighted spin-echo image. On the FLAIR image, the lesion appears larger. Figure 3 shows another example of a lesion with a thin rim of negative phase shift and increased R2*. This rim is not visible on the 3.0-T T1-weighted spin-echo and T2-weighted spin-echo images, possibly because of the reduced contrast and/or the inferior spatial resolution. Another detail lost on the 3.0-T images is the conspicuous veins that appear to traverse many of the lesions on the 7.0-T magnitude and phase images.

Postmortem MR Imaging and Immunohistochemical Analysis

The postmortem study reproduced several of the lesion types seen in vivo (Figs 4–6). As shown in Figure 4, excellent MR imaging quality was obtained in the tissue slabs at 7.0 T, facilitating lesion detection. Two lesion areas selected from these MR images (white rectangles in Fig 4) were further processed for imaging at 11.7 T to obtain the highest contrast and spatial resolution (Figs 5 and 6).

Figure 5 shows a periventricular lesion with strong R2* reduction but close-to-normal phase. This contrast pattern matches that of the dominant in vivo lesion group reported in Table 3, as well as that of the lesions shown in Figure 1. Histochemical staining showed that the R2* reduction was matched by a low content of iron and myelin in the presence of ferritin. Outside the lesions, MR imaging magnitude and R2* showed a robust contrast between gray matter and WM. The histologic stains indicated that both iron and myelin were more concentrated in WM than in gray matter, consistent with the notion that both myelin and iron increase R2*. Ferritin also had a higher concentration in WM, consistent with the distribution of iron. However, this consistency was not seen in the lesion area, where there was reduced iron content but little change in the ferritin content.

In Figure 6, a large MS plaque in the WM between cortical gyri in the temporal lobe can be seen in the magnitude MR image. Negative phase shift and R2* increase are seen at the rim of the lesion, while the lesion center has normal phase and reduced R2*. This rim contrast matches the in vivo finding presented in Figures 2 and 3. Comparison with results of histochemical

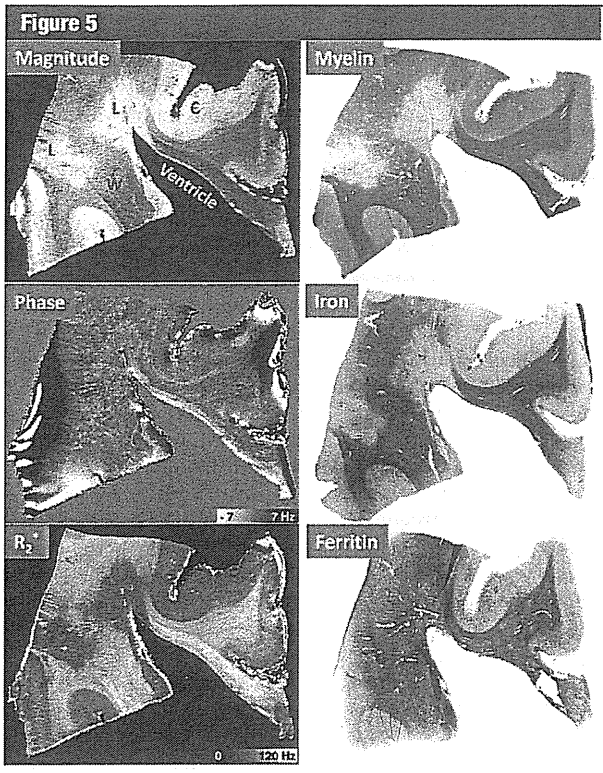

Figure 5: Comparison of 11.7-T MR images (magnitude, phase, and R2*) with results of histochemical stains for myelin, iron, and ferritin in postmortem MS tissue with periventricular lesions. MR imaging parameters were as follows: echo time, 10.4 msec; and spatial resolution, 0.1-mm isotropic. *C* = cortical gray matter, *L* = MS lesion plaque, *W* = WM.

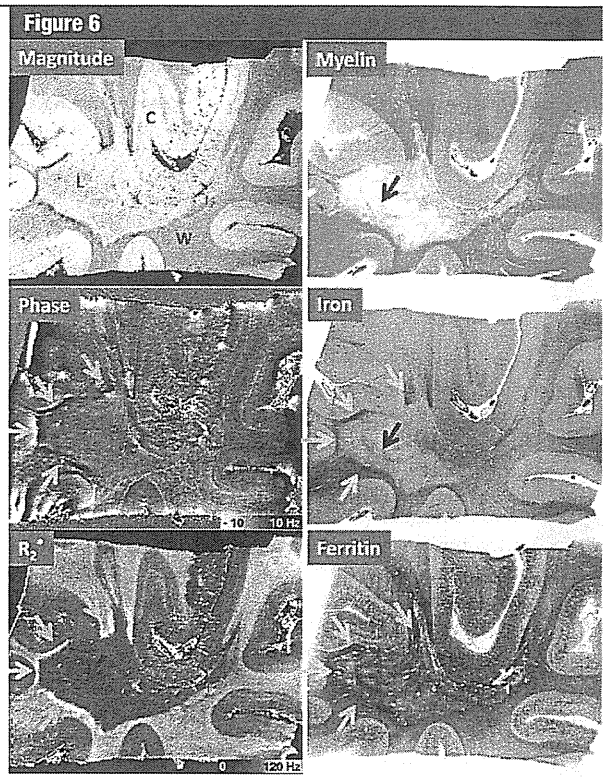

Figure 6: Comparison of 11.7-T MR images (magnitude, phase, and R2*) with results of histochemical stains for myelin, iron, and ferritin in postmortem MS tissue with lesions in the temporal lobe. MR imaging parameters were as follows: echo time, 10.4 msec; and spatial resolution, 0.1-mm isotropic. *C* = cortical gray matter, *L* = MS lesion plaque, *W* = WM. Yellow arrows = areas of large iron deposits at the edge of the lesion. Red arrow = area with preserved iron and myelin inside the lesion.

staining shows that the rim contrast is coincident with a positive Perls stain, suggesting the presence of iron. Notably, the reduced R2* in the center of the lesions coincides with reduced myelin staining and, to a lesser extent, reduced iron staining. This inner portion of the lesion appears to have a thin section of almost normal iron and myelin, which is visible on the R2* map but not in the phase map. Ferritin appears to be increased in the rim and variable in the center of the lesion.

Discussion

Susceptibility-weighted 7.0-T MR imaging data (R2* and phase images) obtained in 21 patients with MS demonstrated highly heterogeneous lesion contrast and revealed lesion details not seen with conventional MR imaging. This heterogeneity was present across and in some cases within lesions. Consistent with previous work (9), lesions with and without pronounced rim contrast were observed. These lesion aspects were reproduced at MR imaging of postmortem tissues. The correlation between MR images and the iron and myelin stains suggests that the varying MR imaging phase and R2* contrast is due to varying levels of iron and myelin.

The appearance of MS lesions often differed between phase and R2* images in our study. Notably, in both in vivo and postmortem images, regions with substantial R2* reduction often had normal phase. Our interpretation is that myelin and iron have a different effect on R2* and phase contrasts. While both iron and myelin increase R2* relaxation rate, myelin may counteract the paramagnetic susceptibility shift associated with iron. This hypothesized diamagnetic shift associated with myelin proposed in our model is consistent with recent high-field-strength MR imaging observations in the line of Gennari, a myelin-rich layer in human primary visual cortex (28), and the absence of phase contrast between cerebrospinal fluid and WM in this and previous work (11), despite the strongly different iron and myelin concentrations of the two substances.

Results of number of recent studies, including iron extraction studies (28,29), demyelinating animal models with shiverer mice (30) and cuprizone-treated mice (31), and correlative studies between MR imaging and histochemically

Table 4

Hypothetical Influence of Tissue Content Change on MR Images

Change in Tissue Content Compared with Normal Tissue	Influence on R2* Signal on MR Images	Influence on Phase Signal on MR Images
Iron increase	Increase	Negative shift (paramagnetic shift)
Iron decrease	Decrease	Positive shift (diamagnetic shift)
Myelin increase	Increase	Positive shift (diamagnetic shift)
Myelin decrease	Decrease	Negative shift (paramagnetic shift)

derived measures of tissue iron (12,20), have suggested that iron and myelin are the main compounds that contribute to the R2* and phase contrast in WM and cortical gray matter. In particular, in the iron extraction experiment, Fukunaga and colleagues (28) reported subtle signs of contrast reversal after iron extraction in postmortem brain tissue, suggesting a small opposing frequency shift caused by the remaining myelin. Furthermore, the sensitivity of MR imaging is adequate to depict even small variations in iron levels. For example, iron levels well below the naturally occurring levels of about 40 μg per gram of tissue in gray matter and WM can be detected, as described previously (28). Therefore, tissue iron increases suggested by the staining data will invariably lead to increases in R2*, except in cases where the iron increase is accompanied by myelin decrease. Conversely, R2* increases, as seen in the rims of ring lesions, result from either iron increases or myelin increases. The latter is highly unlikely, given that MS is a demyelinating disease, and the staining results in our study do not show a myelin increase in the rim.

On the basis of this phenomenon, our tentative interpretation of the MR imaging findings is summarized in Table 4, which describes the results we obtained in the postmortem experiment. In the example of non-ring lesions, reduced R2* and phase cancellation effect were observed inside the lesions because both iron and myelin concentration were low. In the other example, we have found that iron accumulated at the rim of the ring type of lesion, where no prominent myelin deposition was observed. The MR imaging result showed that in this area (high iron, normal myelin), both phase and R2* had a prominent contrast (high R2* values and negative frequency shift). However, in the inner part of the lesion, where iron and myelin were both preserved, an increased R2* but little frequency shift was observed.

The results described in Table 4 allow us to further analyze the in vivo findings summarized in Table 3. Lesions with reduced R2* and normal phase may have substantial reduction in myelin. This tissue loss may lead to a concomitant increase in extracellular space and water accumulation, leading to an increase in T1. This would explain the presence of reduced T1-hypointense signal often associated with these lesions.

Conversely, areas of negative phase shift and normal or increased R2*, often found at the rim and periphery of lesions, may indicate increased iron with relatively preserved myelin content. This is in line with an earlier observation of iron accumulation at the periphery of chronic MS lesions and may indicate ongoing demyelination in the absence of inflammation (21). The methods used in the current study offer the opportunity of detecting this particular disease process in vivo, which may lead to improved characterization of MS in individual patients.

There may be contributions from other compounds as well, but these are most likely to be secondary. One way to establish quantitatively the contribution of iron would be to perform MR imaging before and after chemical extraction of iron. We and others have done this in normal tissue for gray matter and WM (28,29). Despite the lack of these data in the present experiment, the several pieces of circumstantial evidence that we have make it highly likely that iron is the dominant source of the rim contrast.

The precise cellular localization of the iron is an intriguing question and the topic of an ongoing investigation in our group. Several hypotheses may be postulated. First, one can postulate that iron is within macrophage and microglia cells, surrounding the lesions in a ring-like fashion. Second, one can argue that oligodendrocytes are an important source of iron (32–34). Iron in microglia may indicate chronic inflammation, whereas iron in oligodendrocytes has been suggested to support myelin production, as it is a required cofactor for cholesterol and lipid biosynthesis, as well as for support of the oxidative metabolism, which occurs in oligodendrocytes at a higher rate than in other brain cells (35).

In normal brain, much of the nonheme iron that supports oligodendrocytes is stored in ferritin. From our immunochemical ferritin stain results, we could not firmly establish whether this also holds true in MS, as the presence of iron was not always mirrored by that of ferritin and vice versa. The data presented in the current study suggest that in many lesions, ferritin iron may have been effectively removed from the tissue. We explain this finding by hypothesizing that the amount of iron per ferritin molecule may vary and cannot be deduced from the MR imaging data. It is possible that the abnormal iron observed may partly reflect free iron released during either inflammation or demyelination (36).

The formaldehyde fixation process may have effects on the transition metal contents in the brain tissues and has the potential to leach the content of iron. The degree of leaching is time dependent and very different for different elements. A study (37) that used high-spatial-resolution inductively coupled plasma mass spectrometry to measure 19 metal elements in the human brain showed that there was moderate iron leaching after long-term storage (about 20 years), compared with other metal

elements. The concentration of iron in the stored formalin in which the human brains had been stored for years was about 20 times larger than that in the fresh formalin (565 vs 31 μg/L). However, the amount of leached iron was still small compared with the total iron content in the brain (313000 μg/kg dry weight). Another study (38) investigated iron-loaded spleen tissue immersed over a period of 200 days. The result showed that over the first 60 days, there was a steady leakage from the tissue until 3% of the iron had been lost, but thereafter no further leaching was detected. However, a recent experimental approach using atomic absorption spectroscopy (39) revealed that formalin fixation lasting 4 years leads to 43% of the average brain iron reduction. Nevertheless, since the leaching effect is a global effect to the tissue, it may cause some bias but is unlikely to affect the conclusion of our study.

A few limitations of our study need to be addressed. An important one is the fact that only one postmortem brain was available for investigation, which somewhat limits the generalizability of the result. And although multiple lesion areas were examined in the postmortem experiment, not all lesion types seen in vivo were seen in the tissue samples. Thus, questions remain regarding the other lesion types not present in the postmortem data. Second, it is important to consider that besides iron and myelin, other factors such as fiber orientation and tissue microstructure may play a role in contribution to the image contrast. A third limitation was the current lack of information about the cellular localization of the iron. Although it is generally assumed that most iron in normal brain is present in the form of storage iron in hemosiderin and ferritin molecules (40), it would be interesting to find out whether this continues to be the case in diseases such as MS and whether this storage occurs in microglia, astrocytes, or other cell types. The latter was outside the focus of the present investigation, which was limited to establishing the role of iron and myelin in the generation of susceptibility contrast in MS tissues.

In conclusion, the data presented in this work suggest that the combined use of R2* and phase data may allow distinction between changes in tissue myelin and iron associated with MS, and this distinction, combined with the increased spatial resolution and contrast available with high-field-strength MR imaging, may provide great help in characterizing the disease process underlying MS lesions.

Acknowledgments: We thank Drs Xin Yu and Steve Dodd for their assistances with the imaging at 11.7 T. We thank Joan Ohayon, CRNP, and Helen Griffith, RN, as well as our patient coordinator, Melissa Goldstein, BS, for assistance with patients.

Disclosures of Potential Conflicts of Interest: **B.Y.** No potential conflicts of interest to disclose. **F.B.** No potential conflicts of interest to disclose. **E.M.** No potential conflicts of interest to disclose. **H.M.** No potential conflicts of interest to disclose. **P.v.G.** No potential conflicts of interest to disclose. **F.K.C.** No potential conflicts of interest to disclose.

References

1. Gilmore CP, DeLuca GC, Bö L, et al. Spinal cord neuronal pathology in multiple sclerosis. Brain Pathol 2009;19(4):642–649.
2. Bagnato F, Yao B, Cantor F, et al. Multisequence-imaging protocols to detect cortical lesions of patients with multiple sclerosis: observations from a post-mortem 3 Tesla imaging study. J Neurol Sci 2009;282(1-2):80–85.
3. Goldberg-Zimring D, Mewes AU, Maddah M, Warfield SK. Diffusion tensor magnetic resonance imaging in multiple sclerosis. J Neuroimaging 2005;15(4,Suppl):68S–81S.
4. Parry A, Clare S, Jenkinson M, Smith S, Palace J, Matthews PM. White matter and lesion T1 relaxation times increase in parallel and correlate with disability in multiple sclerosis. J Neurol 2002;249(9):1279–1286.
5. Bakshi R, Benedict RH, Bermel RA, et al. T2 hypointensity in the deep gray matter of patients with multiple sclerosis: a quantitative magnetic resonance imaging study. Arch Neurol 2002;59(1):62–68.
6. Laule C, Vavasour IM, Moore GR, et al. Water content and myelin water fraction in multiple sclerosis: a T2 relaxation study. J Neurol 2004;251(3):284–293.
7. Karampekios S, Papanikolaou N, Papadaki E, et al. Quantification of magnetization transfer rate and native T1 relaxation time of the brain: correlation with magnetization transfer ratio measurements in patients with multiple sclerosis. Neuroradiology 2005;47(3):189–196.
8. Chen JT, Kuhlmann T, Jansen GH, et al. Voxel-based analysis of the evolution of magnetization transfer ratio to quantify remyelination and demyelination with histopathological validation in a multiple sclerosis lesion. Neuroimage 2007;36(4):1152–1158.
9. Hammond KE, Metcalf M, Carvajal L, et al. Quantitative in vivo magnetic resonance imaging of multiple sclerosis at 7 Tesla with sensitivity to iron. Ann Neurol 2008;64(6):707–713.
10. Haacke EM, Makki M, Ge Y, et al. Characterizing iron deposition in multiple sclerosis lesions using susceptibility weighted imaging. J Magn Reson Imaging 2009;29(3):537–544.
11. Duyn JH, van Gelderen P, Li TQ, de Zwart JA, Koretsky AP, Fukunaga M. High-field MRI of brain cortical substructure based on signal phase. Proc Natl Acad Sci U S A 2007;104(28):11796–11801.
12. Li TQ, Yao B, van Gelderen P, et al. Characterization of T(2)* heterogeneity in human brain white matter. Magn Reson Med 2009;62(6):1652–1657.
13. Haacke EM, Cheng NY, House MJ, et al. Imaging iron stores in the brain using magnetic resonance imaging. Magn Reson Imaging 2005;23(1):1–25.
14. Ogg RJ, Langston JW, Haacke EM, Steen RG, Taylor JS. The correlation between phase shifts in gradient-echo MR images and regional brain iron concentration. Magn Reson Imaging 1999;17(8):1141–1148.
15. Sedlacik J, Helm K, Rauscher A, Stadler J, Mentzel HJ, Reichenbach JR. Investigations on the effect of caffeine on cerebral venous vessel contrast by using susceptibility-weighted imaging (SWI) at 1.5, 3 and 7 T. Neuroimage 2008;40(1):11–18.
16. Zhong K, Leupold J, von Elverfeldt D, Speck O. The molecular basis for gray and white matter contrast in phase imaging. Neuroimage 2008;40(4):1561–1566.
17. He X, Yablonskiy DA. Biophysical mechanisms of phase contrast in gradient echo MRI. Proc Natl Acad Sci U S A 2009;106(32):13558–13563.
18. Schäfer A, Wharton S, Gowland P, Bowtell R. Using magnetic field simulation to study susceptibility-related phase contrast in gradient echo MRI. Neuroimage 2009;48(1):126–137.
19. Lee J, Hirano Y, Fukunaga M, Silva AC, Duyn JH. On the contribution of deoxyhemoglobin to MRI gray-white matter phase contrast at high field. Neuroimage 2010;49(1):193–198.

20. Yao B, Li TQ, Gelderen P, Shmueli K, de Zwart JA, Duyn JH. Susceptibility contrast in high field MRI of human brain as a function of tissue iron content. Neuroimage 2009; 44(4):1259–1266.

21. Craelius W, Migdal MW, Luessenhop CP, Sugar A, Mihalakis I. Iron deposits surrounding multiple sclerosis plaques. Arch Pathol Lab Med 1982;106(8):397–399.

22. Polman CH, Reingold SC, Edan G, et al. Diagnostic criteria for multiple sclerosis: 2005 revisions to the "McDonald Criteria". Ann Neurol 2005;58(6):840–846.

23. Kurtzke JF. Rating neurologic impairment in multiple sclerosis: an expanded disability status scale (EDSS). Neurology 1983;33(11): 1444–1452.

24. van Gelderen P, de Zwart JA, Starewicz P, Hinks RS, Duyn JH. Real-time shimming to compensate for respiration-induced B0 fluctuations. Magn Reson Med 2007;57(2): 362–368.

25. de Zwart JA, Ledden PJ, van Gelderen P, Bodurka J, Chu R, Duyn JH. Signal-to-noise ratio and parallel imaging performance of a 16-channel receive-only brain coil array at 3.0 Tesla. Magn Reson Med 2004;51(1): 22–26.

26. Filippi M, Gawne-Cain ML, Gasperini C, et al. Effect of training and different measurement strategies on the reproducibility of brain MRI lesion load measurements in multiple sclerosis. Neurology 1998;50(1):238–244.

27. Bagnato F, Jeffries N, Richert ND, et al. Evolution of T1 black holes in patients with multiple sclerosis imaged monthly for 4 years. Brain 2003;126(Pt 8):1782–1789.

28. Fukunaga M, Li TQ, van Gelderen P, et al. Layer-specific variation of iron content in cerebral cortex as a source of MRI contrast. Proc Natl Acad Sci U S A 2010;107(8):3834–3839.

29. Schenck JF, Zimmerman EA, Li Z, et al. High-field magnetic resonance imaging of brain iron in Alzheimer disease. Top Magn Reson Imaging 2006;17(1):41–50.

30. Liu C, Li W, Johnson GA, Wu B. High-field (9.4 T) MRI of brain dysmyelination by quantitative mapping of magnetic susceptibility. Neuroimage 2011;56(3):930–938.

31. Lee J, Yao B, Palumbo S, et al. MRI T2* relaxation and frequency contrast changes in cuprizone-fed mice. 17th Organization for Human Brain Mapping Annual Meeting, Quebec City, Canada, 2011.

32. Dietrich RB, Bradley WG Jr. Iron accumulation in the basal ganglia following severe ischemic-anoxic insults in children. Radiology 1988;168(1):203–206.

33. Schenck JF. Imaging of brain iron by magnetic resonance: T2 relaxation at different field strengths. J Neurol Sci 1995;134(Suppl): 10–18.

34. Connor JR, Menzies SL, St Martin SM, Mufson EJ. A histochemical study of iron, transferrin, and ferritin in Alzheimer's diseased brains. J Neurosci Res 1992;31(1):75–83.

35. Connor JR, Menzies SL. Relationship of iron to oligodendrocytes and myelination. Glia 1996;17(2):83–93.

36. Levine SM, Chakrabarty A. The role of iron in the pathogenesis of experimental allergic encephalomyelitis and multiple sclerosis. Ann N Y Acad Sci 2004;1012:252–266.

37. Gellein K, Flaten TP, Erikson KM, Aschner M, Syversen T. Leaching of trace elements from biological tissue by formalin fixation. Biol Trace Elem Res 2008;121(3):221–225.

38. Chua-anusorn W, Webb J, Macey DJ, Pootrakul P, St Pierre TG. The effect of histological processing on the form of iron in iron-loaded human tissues. Biochim Biophys Acta 1997;1360(3):255–261.

39. Schrag M, Dickson A, Jiffry A, Kirsch D, Vinters HV, Kirsch W. The effect of formalin fixation on the levels of brain transition metals in archived samples. Biometals 2010;23(6):1123–1127.

40. Schenck JF. Magnetic resonance imaging of brain iron. J Neurol Sci 2003;207(1-2): 99–102.